Chemical Science
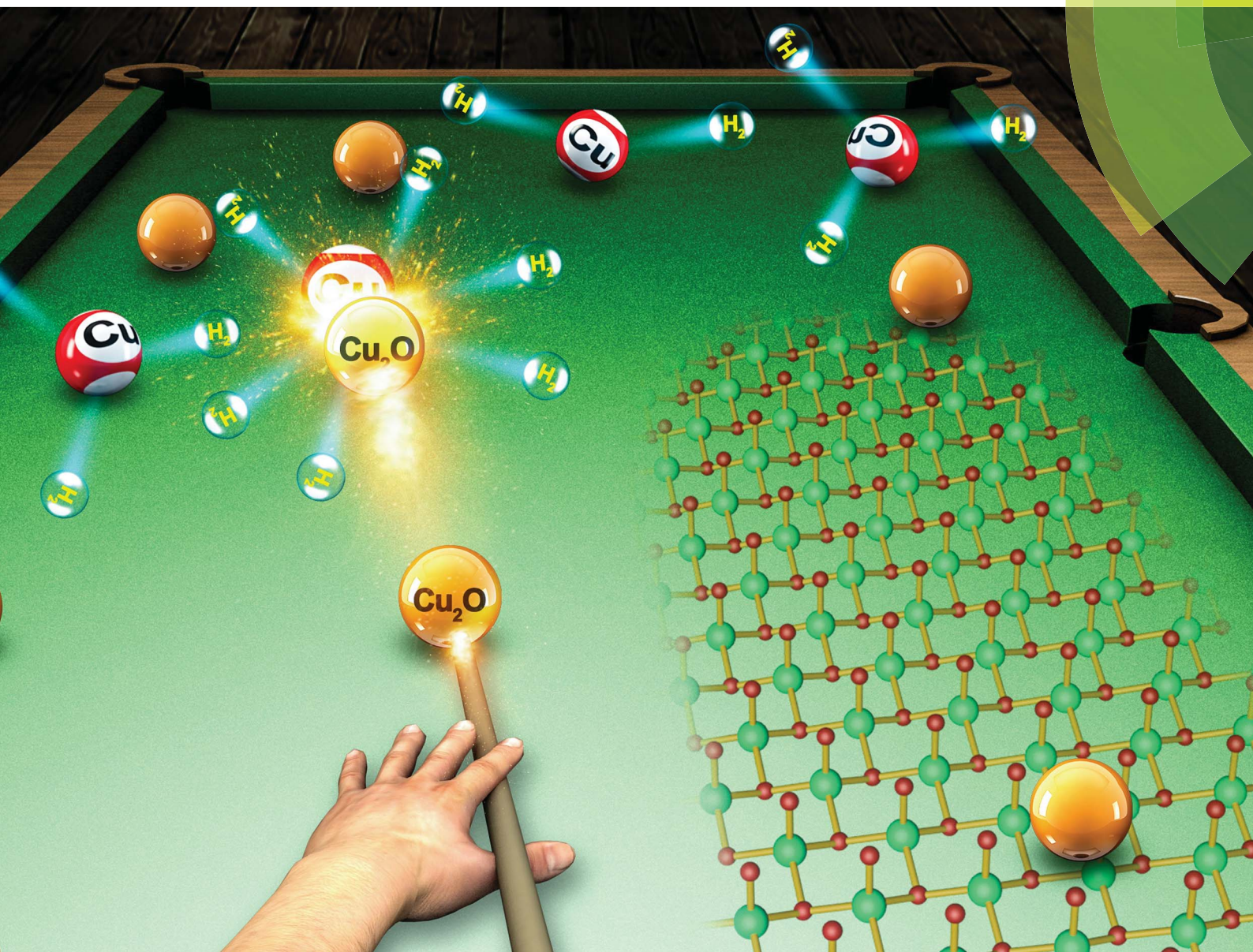
rsc.li/chemical-science

ROYAL SOCIETY OF CHEMISTRY | Celebrating **IYPT** 2019

EDGE ARTICLE
Jinlong Gong, Xingang Li *et al.*
Achieving efficient and robust catalytic reforming on dual-sites of Cu species

EDGE ARTICLE

Check for updates

Achieving efficient and robust catalytic reforming on dual-sites of Cu species†

Kui Ma,[ab] Ye Tian,[ab] Zhi-Jian Zhao,[ac] Qingpeng Cheng,[ab] Tong Ding,[ab] Jing Zhang,[d] Lirong Zheng, [d] Zheng Jiang,[e] Takayuki Abe,[f] Noritatsu Tsubaki, [g] Jinlong Gong [*ac] and Xingang Li [*ab]

Catalytic reforming provides a practical technique for on-board hydrogen production in fuel cell applications. The high energy density, easy transportation and non-toxicity of biomass-derived dimethyl ether (bio-DME) offer potential to replace methanol for on-board steam reforming (SR). Presently, the reaction mechanism over conventional Cu-based SR catalysts remains elusive, limiting the rational design of highly efficient reforming systems. Herein, we build a catalytic system for bio-DME SR with dual-sites of Cu species, *i.e.*, Cu^+ and Cu^0 sites, and achieve a record-high H_2 production rate of 1145 mol kg_{cat}^{-1} h^{-1}. *Via* regulating the ratios of the dual-sites of Cu, we clearly describe molecular understandings on SR. And we discover that the substantially boosted activity is induced by a new Cu^+-determined reaction path substituting the conventional Cu^0-determined path. Intrinsically, Cu_2O can act as a physical spacer and hydroxyl consumer to suppress the aggregation of metallic Cu species in SR. Due to the unique structure of metallic Cu surrounded by Cu_2O, the catalyst exhibits robust catalytic performance even after severe thermal treatment. These findings open a new avenue for designing efficient catalytic reforming systems with commercial potential.

Introduction

Hydrogen, a renewable resource with a high energy density (142 MJ kg^{-1}), is consumed today as a chemical raw material (about 5×10^{10} kg per year worldwide).[1] As the core of the hydrogen economy, fuel cells running on hydrogen are attractive power supplies for versatile applications.[2,3] The required hydrogen comes from a stable on-board production system, ensuring its safe storage and transportation.[4,5] Recently, the development of technologies for converting biomass has resuscitated the surge of reforming renewable oxygenated hydrocarbons, *e.g.*,

methanol, ethanol, dimethyl ether (DME), and glycerol, with H_2O for on-board hydrogen production.[6–8] In view of the mild SR conditions, methanol and DME without C–C bonds are the primary choices.[9] The usage of DME can release hydrogen with a higher gravimetric density of 26.1 wt% than methanol (18.8 wt%). As the European project BioDME has been industrially built and operated in Sweden, bio-DME is becoming a potential reforming feed to replace the traditional methanol.[10,11] The non-toxicity of DME offers another important advantage. DME SR is an integrated technology consisting of hydrolysis of DME to methanol over solid acid catalysts, and subsequently methanol SR over metal catalysts. Currently, γ-Al_2O_3 is the commonly used acid catalyst for DME hydrolysis operated above 300 °C,[12] requiring higher operating temperatures for the following SR. And copper-based catalysts have been intensively explored in reforming reactions with the inherent drawback of thermal deactivation by metal-particle growth.[13]

It is commonly perceived that Cu^0 is primary and indispensable for SR,[14,15] bringing debate about the role of Cu^+. Some researchers have proposed that Cu^+ is active in suppressing the by-product of carbon monoxide (CO) from the reverse water–gas shift, the main side reaction in SR.[16–18] However, others still suggest that Cu^+ could directly catalyze the steam reforming, and speculate that there may exist an optimum cooperation between Cu^0 and Cu^+ to boost activities,[19–21] but this lacks effective evidence. Currently, Cu^+ species are usually introduced through addition of metal oxides to Cu-based catalysts, and self-

[a]School of Chemical Engineering & Technology, Tianjin University, Collaborative Innovation Center of Chemical Science and Engineering (Tianjin), Tianjin 300072, China. E-mail: jlgong@tju.edu.cn; xingang_li@tju.edu.cn

[b]Tianjin Key Laboratory of Applied Catalysis Science & Engineering, Tianjin 300072, China

[c]Key Laboratory for Green Chemical Technology of Ministry of Education, Tianjin 300072, China

[d]Beijing Synchrotron Radiation Facility, Institute of High Energy Physics, Chinese Academy of Sciences, Beijing 100049, China

[e]Shanghai Synchrotron Radiation Facility, Shanghai Institute of Applied Physics, Chinese Academy of Sciences, Shanghai 201800, China

[f]Hydrogen Isotope Research Center, University of Toyama, Gofuku 3190, Toyama 930-8555, Japan

[g]Department of Applied Chemistry, School of Engineering, University of Toyama, Gofuku 3190, Toyama 930-8555, Japan

† Electronic supplementary information (ESI) available. See DOI: 10.1039/c9sc00015a

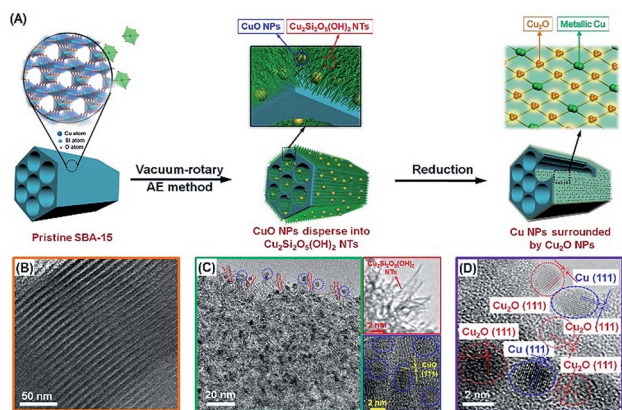This journal is © The Royal Society of Chemistry 2019
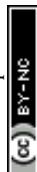
Fig. 1 (A) Schematic procedure for the synthesis of the Cu-AE catalysts; TEM images of (B) the pristine SBA-15, and (C) calcined and (D) reduced 25Cu-AE catalyst.

redox reaction of copper species under feed and reaction conditions.[22–25] The complexity of these systems impairs efforts to identify the exact role of copper. In this regard, copper phyllosilicates [$Cu_2Si_2O_5(OH)_2$], providing stable Cu^+ species under hydrogen-rich conditions in catalytic hydrogenation,[26–28] may be adopted as a controllable Cu^+-supplier to investigate SR mechanisms. However, the tendency of Cu nanoparticles (NPs) to grow into larger crystallites is an impediment to the stable performance of Cu-based catalysts, especially for those without promoters. Intrinsically below the Tammann temperature of copper (407 °C), the aggregation of Cu NPs is mainly induced by Ostwald ripening occurring across the support surface through the functional groups (e.g., hydroxyl).[29] It is another stumbling block in further design of Cu-based catalysts.

This paper describes the design and fabrication of a hierarchical Cu–Si system with dual-sites of Cu species (denoted as Cu-AE) via a vacuum-rotary ammonia evaporation method by employing SBA-15 as the silicon source. The ordered three-dimensional (3D) mesoporous channels of SBA-15 can improve molecular diffusion, and restrict the growth of copper NPs. As described in Fig. 1A, the well-ordered ≡Si–OH sites on SBA-15 and vacuum conditions facilitate the dispersion and uniform arrangement of the Cu species.[30] Consequently, CuO nanoparticles (NPs) dispersed into $Cu_2Si_2O_5(OH)_2$ nanotubes (NTs) are successfully developed on SBA-15. After reduction, metallic Cu NPs are generated from the CuO NPs, while the Cu_2O NPs are from the surrounding $Cu_2Si_2O_5(OH)_2$ NTs. Based on this synthesis mechanism, we tune the dual-sites of copper to quantify their contributions to SR, and achieve a record-high H_2 production rate of 1145 mol kg_{cat}^{-1} h^{-1} with the structure of metallic Cu surrounded by Cu_2O. We also discover that the formation of Cu_2O consumes the hydroxyl groups on the support, which retards the Ostwald ripening of metallic Cu, thereby leading to a robust SR performance.

Results and discussion

The TEM images of 25Cu-AE in Fig. 1B–D are obtained to illustrate the synthetic procedure. As indicated by the FTIR and UV-Raman results (Fig. S1†), abundant ≡Si–OH groups (the ν_{Si-OH} vibration at 958 cm^{-1})[31] exist on the SiO_4 tetrahedron-shaped matrix of the mesoporous SBA-15 (Fig. 1B). After ammonia evaporation, the disappearance of the ν_{Si-OH} vibration band in 25Cu-AE implies that the ≡Si–OH groups are consumed during the $Cu_2Si_2O_5(OH)_2$ formation. On 25Cu-AE, the NPs are CuO, while the NTs lacking lattice fringes are $Cu_2Si_2O_5(OH)_2$ (Fig. 1C).[32] This formation mechanism is also applied to the other Cu-AE catalysts with different Cu loadings. The XRD and X-ray absorption near-edge structure (XANES) results also verify the coexistence of $Cu_2Si_2O_5(OH)_2$ and CuO in Cu-AE catalysts (Fig. S2†).[27]

Semi-quantitatively, we adopted linear combination fitting (LCF) of the XANES spectra (Fig. S3†) to estimate the contents of $Cu_2Si_2O_5(OH)_2$ in the catalysts. It shows a volcano-type behavior following the increase of the Cu content and maximizes at 25Cu-AE (Table S1†). Obviously, in Fig. S4A,† CuO NPs are continuously enriched with the increase of the copper content in the catalysts, and eventually cap the $Cu_2Si_2O_5(OH)_2$ NTs. From the low-angle XRD patterns in Fig. S5,† all the samples present three well-resolved diffractions at a 2θ of 0.5–3.0, which can be indexed to the ordered hexagonal lattice (p6mm) of SBA-15.[30] Noticeably, the diffraction peaks of the Cu-AE catalysts shift to higher angles compared with those of the pristine SBA-15, reflecting a slight contraction of the unit cell. This phenomenon is contributed by the partial destruction of the ordered pore structure of SBA-15 due to the dissolution of silica during the preparation process, as can be directly observed by TEM as shown above. Here, the existence of these characteristic low-angle diffraction peaks of Cu-AE suggests that most of the channels of SBA-15 are still preserved. Furthermore, the Cu-AE catalysts show weaker d_{100} intensity, indicating that the copper loading in the mesopore channels reduces X-ray diffraction.[33,34] Based on the above results, the schematic illustrations of the Cu species distribution with the increased Cu loading are presented in Fig. S4C.† Summarily, the 25Cu-AE possesses the well-proportioned and uniformly arranged $Cu_2Si_2O_5(OH)_2$ NTs and CuO NPs.

In the reduced Cu-AE catalysts, both the preserved characteristic diffractions of SBA-15 in low-angle XRD patterns (Fig. S6A†) and the narrowed size distribution of 4.3 nm (Fig. S7†) demonstrate the existence of regular channels. We also observed Cu_2O (JCPDS no. 05-0667) and metallic Cu (JCPDS no. 04-0836) from wide-angle XRD patterns in Fig. S6B.† Cu_2O and metallic Cu originate from the reduction of $Cu_2Si_2O_5(OH)_2$ and CuO, respectively.[27] In particular, the metallic Cu is surrounded by Cu_2O on 25Cu-AE (Fig. 1D), which is due to the appropriate proportion of Cu species in the calcined catalysts (Fig. S4†). Table S2† gives the physicochemical properties of the catalysts, indicating that we can modulate the physicochemical properties of Cu-AE via tuning the Cu loading. Compared with other catalysts, the Cu-AE catalysts possess the smaller Cu crystal sizes and more accessible surface Cu atoms.

We employed H_2-TPR (Fig. 2A) and in situ reduction QXAFS (Fig. 2B) to identify the reducibility and copper species of the catalysts. Generally, the reduction of copper phyllosilicates to Cu^+ and highly dispersed CuO to Cu^0 occurs at ca. 247–267 °C
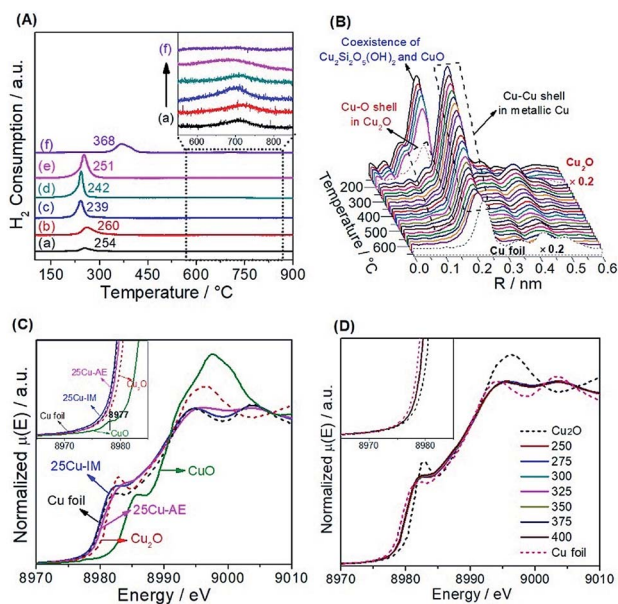
Fig. 2 (A) H_2-TPR profiles of (a) 10Cu-AE, (b) 20Cu-AE, (c) 25Cu-AE, (d) 30Cu-AE, (e) 40Cu-AE, and (f) 25Cu-IM; the inset shows the reduction of Cu^+ in copper phyllosilicates; (B) temperature-resolved *in situ* RSFs of the Cu K-edge for 25Cu-AE in 5% H_2/N_2 from RT to 650 °C; (C) *in situ* steady-state XANES spectra of the Cu K-edge for the reduced 25Cu-AE and 25Cu-IM catalysts in 5% reactants ($n(CH_3OH)/n(H_2O) = 1/2$) in N_2 at 400 °C; the inset shows the amplified curves; (D) *in situ* temperature-resolved XANES spectra of the Cu K-edge for the reduced 25Cu-AE catalyst under reaction conditions: 5% reactants ($n(CH_3OH)/n(H_2O) = 1/2$) in N_2, from 250 to 400 °C with an interval of 25 °C; the inset shows the amplified curves.

(ref. 28) and 237 °C,[35] respectively. Thus, we attribute the single peak below 300 °C here to the overlap of these two reduction processes. Correspondingly in this range, we observe the co-existence of Cu_2O with the first Cu–O coordination (*ca.* 0.15 nm) and metallic Cu with the first Cu–Cu coordination (*ca.* 0.20 nm). The existence of Cu^+ in the reduced Cu-AE catalysts is also verified by the Cu^+-carbonyl band (2122 cm^{-1}) observed from the *in situ* DRIFTS spectrum of CO adsorption (Fig. S8†). Notably, the broadening peaks above 600 °C (inset in Fig. 2A) indicate the further reduction of Cu^+ to metallic Cu.[35] Simultaneously, the Cu–O coordination peaks decrease, also indicating the gradual reduction of the Cu species to Cu^0 as shown in Fig. 2B. For 25Cu-IM, the main reduction peak at *ca.* 368 °C is assigned to the reduction of large CuO particles to metallic Cu.[26]

We also distinguished the superficial copper species of Cu^+ and Cu^0 using the Cu LMM Auger kinetic energy peaks[36] at *ca.* 915.5 and 919.0 eV, respectively, for the reduced catalysts (Fig. S9†). The modified Auger parameter (A.P.) values, which represent the summation of the kinetic energy of the Cu LMM Auger electron and the binding energy of the Cu $2p_{3/2}$ photo-electron, are calculated and summarized in Table S3.† The smaller A.P. values of Cu^+ here (*ca.* 1848.5 eV) than that of the Cu_2O bulk (*ca.* 1849.0 eV)[36] are attributed to the electron transfer from Cu^+ to SBA-15, inducing a strong interaction to keep the Cu^+ stable. Moreover, the Cu 2p XPS spectra (Fig. S10†) before and after a single reaction cycle indicates that the change

in the chemical environment and content of surface Cu (Table S3†) are nearly negligible, also suggesting that the equilibrium between Cu^+ and Cu^0 over the reduced Cu-AE catalysts is very stable, and is broken with difficulty by the SR reaction. In addition, as summarized in Table S3,† the ratio of $Cu^+/(Cu^0 + Cu^+)$ decreases with the elevated Cu loading, coinciding with the tendency of calculated surface Cu atoms in Table S2.†

Generally, the chemical state of Cu species is sensitive to the environmental atmosphere.[37] We performed *in situ* steady-state XANES to monitor the chemical state of Cu under reaction conditions. As calibrated by the first derivatives of the K-edge XANES spectra in Fig. S11,† the absorption edge at *ca.* 8980.4 eV of 25Cu-AE in Fig. 2C is located in the middle of those of Cu foil (8979.4 eV) and Cu_2O (8980.9 eV). Combined with the absence of the pre-edge feature at *ca.* 8977 eV for Cu^{2+} (inset in Fig. 2C),[38] we conclude that Cu^+ species indeed exist in 25Cu-AE and remain stable during the operation. But for 25Cu-IM, its absorption edge location and white line feature are close to Cu foil, indicating the lack of Cu^+ in the bulk of 25Cu-IM during the reaction. Fig. 2D shows the *in situ* temperature-resolved XANES spectra of 25Cu-AE. The curves are quite similar in shape at different reaction temperatures, and their absorption edges locate in the middle of those of Cu foil and Cu_2O. These results demonstrate that the copper oxidation state has little change in dynamic reactive atmospheres at different reaction temperatures, in accordance with the XPS results in Fig. S9, S10 and Table S3.† The above comprehensive characterization results demonstrate a successful synthesis of the catalytic system with tuneable and stable dual-sites of Cu species.

We investigated the catalytic performance and stability of the catalysts after 12 h severe thermal treatment (GHSV = 36 000 h^{-1}, $T = 450$ °C) for DME SR. Table 1 summarizes the performance of the catalysts in a numerical form, and Table S4† lists the activity of the representative catalysts for DME SR and methanol SR. In Table 1, 25Cu-AE exhibits a higher catalytic activity in comparison with others. It achieves a DME conversion of 100%, CO selectivity of *ca.* 10%, and H_2 yield exceeding 95%, leading to a record-high H_2 production rate of 1145 mol_{H_2} $kg_{cat}^{-1} h^{-1}$ (Table S4†), 6-fold higher than that of commercial CuZnAl.[39] The highest TOF_{H_2} over 25Cu-AE reaches 0.147 s^{-1}, about 2 and 10 times higher than those of the as-prepared Cu/ZnO/Al_2O_3 and 25Cu-IM, respectively (Table 1). Additionally, 25Cu-IM shows a lower H_2 yield and higher CO selectivity as compared with the Cu-AE catalysts, indicating that the latter's excellent catalytic activities probably lie in the presence of Cu^+ species.

Fig. 3A displays the catalytic stability of 25Cu-AE, and Fig. 3B shows the TEM images at the corresponding stages. At stage I prior to the thermal treatment, the activity of 25Cu-AE shows no change while that of 25Cu-SiO_2 drops rapidly as shown in Fig. S12.† Intrinsically, unlike the steady Cu NP distribution of ~3.5 nm over 25Cu-AE (Fig. S13A†), the Cu NPs over 25Cu-SiO_2 increase from ~4.1 to ~9.2 nm (Fig. S13B†) after stage I.

As the reaction temperature (400 °C) is relatively lower than the Tammann temperature of copper (407 °C), the thermal migration of copper atoms in the catalysts is difficult in the absence of a reactive adsorbate. Thus, the copper particle

Table 1 Catalytic performance for DME SR

Catalysts	Conv. (%)	Y (%)	Sel. (%)				$TOF_{H_2}{}^b$ ($s^{-1} \times 10^{-2}$)	$TOF_{DME}{}^c$ ($s^{-1} \times 10^{-3}$)
	DME	H_2	CO	CO_2	CH_4	CH_3OH		
$10Cu\text{-}AE^a$	58.3 ± 6.8	51.6 ± 9.3	12.5 ± 6.3	85.8 ± 7.9	1.7 ± 0.3	—	7.9 ± 0.4	3.0 ± 0.7
$20Cu\text{-}AE^a$	89.0 ± 0.6	80.9 ± 3.3	13.4 ± 3.8	86.3 ± 3.9	0.3 ± 0.1	—	12.1 ± 0.5	8.3 ± 0.8
$25Cu\text{-}AE^a$	100.0 ± 0.0	95.0 ± 1.5	10.4 ± 3.0	89.3 ± 2.9	0.3 ± 0.1	—	14.7 ± 0.9	12.2 ± 0.3
$30Cu\text{-}AE^a$	96.7 ± 0.7	85.4 ± 2.5	12.4 ± 0.8	87.4 ± 2.0	0.2 ± 0.1	—	11.3 ± 1.0	9.2 ± 0.4
$40Cu\text{-}AE^a$	77.5 ± 2.4	69.4 ± 4.0	31.5 ± 7.2	68.0 ± 7.5	0.5 ± 0.2	—	6.1 ± 1.1	6.0 ± 0.9
$25Cu\text{-}IM^a$	16.0 ± 0.6	12.5 ± 0.7	41.5 ± 5.9	57.9 ± 6.7	0.6 ± 0.2	5.5×10^{-2}	1.5 ± 0.4	1.9 ± 0.6
$Cu/ZnO/Al_2O_3{}^a$	92.6 ± 0.1	73.6 ± 2.3	20.3 ± 3.2	79.7 ± 4.0	0.2 ± 0.1	—	7.2 ± 0.7	4.4 ± 0.9

^{a} Reaction conditions: gas hourly space velocity (GHSV) = 18 000 h^{-1}, steam-to-carbon ratio (S/C) = 2/1, T = 400 °C. ^{b} TOF_{H_2} based on the Cu^0 surface area and yield of H_2 at 350 °C. ^{c} TOF_{DME} based on the total Cu surface areas and conversion of DME at 350 °C.
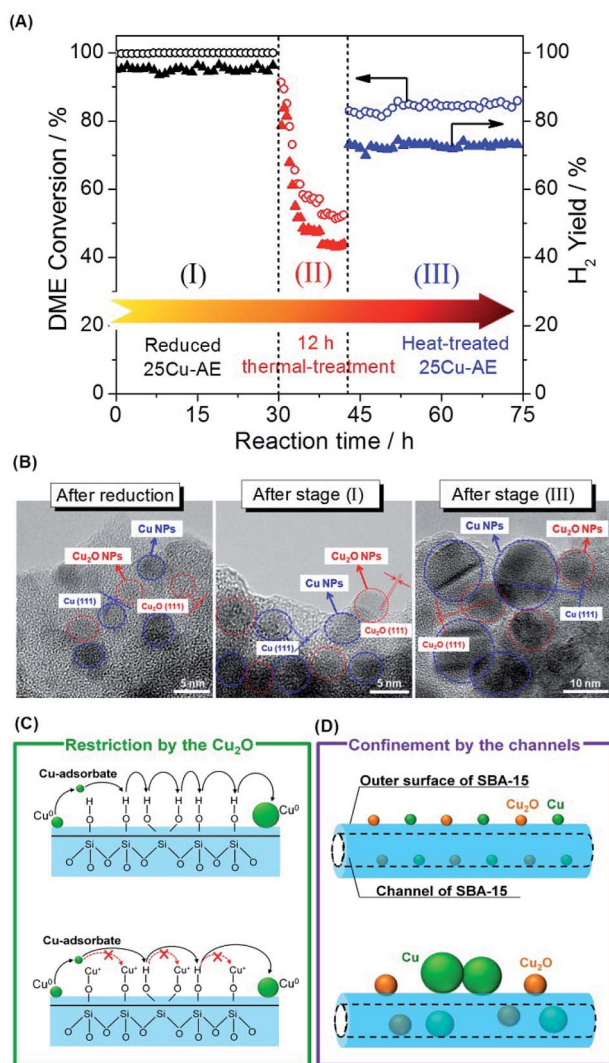

Fig. 3 (A) Stabilities of 25Cu-AE upon thermal treatment. Reaction conditions: (I) and (III): GHSV = 18 000 h^{-1}, S/C = 2/1 (mol mol^{-1}), T = 400 °C; (II): GHSV = 36 000 h^{-1}, S/C = 2/1 (mol mol^{-1}), T = 450 °C; (B) TEM images of 25Cu-AE during the stability test; (C) schematic representation of the restriction by the adjacent Cu_2O; (D) schematic illustration of the spatial confinement by the channels.

growth in SR is probably mediated by mobile copper adsorbate species on the support (Ostwald ripening).[29] The transport of Ostwald ripening Cu species depends upon the chemical nature of the support surface. As evidenced by FTIR in Fig. S1A,† the formation of copper phyllosilicates is accompanied by consuming surface hydroxyl groups, which is an efficient support functionalization to increase the distance between neighboring functional groups and consequently inhibits Cu^0 diffusion, as presented in Fig. 3C. Accordingly, the structure of Cu surrounded by Cu_2O in 25Cu-AE maximizes such restriction. Also, Cu_2O NPs can function as a physical spacer to isolate Cu^0 NPs.

After the thermal treatment (stage II), the DME conversion over 25Cu-AE drops to 84% but remains stable for another 30 h at stage III; meanwhile the TEM images of 25Cu-AE in Fig. 3B demonstrate a break of the surrounding structure of copper species. Herein, a bimodal size distribution of ∼11.2 and ∼5.8 nm is presented after stage III, which is attributed to the aggregated Cu species on the outer surface and in the channels, respectively (Fig. S13A†). For 25Cu-SiO₂, the catalytic performance substantially decreases at stage III. The corresponding Cu NPs noticeably aggregate as indicated by a distribution of ∼15.0 nm after stage III (Fig. S13B†). Thus, we conclude that the spatial restriction by the channels of SBA-15 can also help inhibit the aggregation of Cu^0 (Fig. 3D). Owing to such combined effects, 25Cu-AE exhibits a robust performance (DME conversion: 83.9%, H_2 yield: 72.7%) even after the severe thermal treatment.

We hypothesize that the high activity of Cu-AE results from a cooperative effect of the unique dual-sites of copper species. To gain more insight into this, the respective contributions from the Cu^0 and Cu^+ species are required to be clarified. Thus catalysts containing pure Cu^0 and Cu^+ species are desired. However, the Cu^0 and Cu^+ always coexist in Cu-AE catalysts. For the above compared 25Cu-IM, its crystal size (29 nm) is much larger and less uniform than those of Cu-AE (<10 nm) (Table S2†). Moreover, the impregnation method inevitably brings the strong metal–support interaction to affect the chemical state and size distribution of copper. Consequently, we introduce a physical-sputtering method[40] to realize a homogeneously distributed metallic Cu nano-catalyst (Cu-SP) instead of 25Cu-IM for rigorous comparison and discussion. For Cu-SP, the

TEM and H_2-TPR results (Fig. S14†) show that the copper NPs mainly exist as Cu^0, which could be oxidized to Cu_2O by N_2O to obtain Cu-SP-N. Their physicochemical properties are listed in Table S5.†

We quantify the surface density of Cu^+ and Cu^0 sites (Tables S2 and S5†) to analyze their contributions toward the reaction. In Fig. 4A, the surface Cu^0 site density is observed to scale linearly with the formation rates of H_2 (r_{H_2}) in group I and II independently, suggesting that the H_2 yield depends on the Cu^0 density with two different reaction paths, whereas there is no clear correlation between the r_{H_2} and the total Cu density (Fig. 4B). Moreover, the higher superficial $Cu^+/(Cu^0 + Cu^+)$ ratio (>0.50) over the catalysts in group I than that (<0.21) in group II is probably the main reason for their superior performance. Thus, we conclude that Cu^0 is responsible for H_2 desorption, and sufficient Cu^+ can accelerate the reaction rate. In Fig. 4C, both the TOF_{DME} and TOF_{H_2} show a volcanic correlation with the increased $Cu^0/(Cu^0 + Cu^+)$ ratio, and reach a maximum at a $Cu^0/(Cu^0 + Cu^+)$ ratio equal to 0.50 (25Cu-AE). The activation energies (E_a) of the catalysts were calculated and classified into two types in Fig. 4D: the lower value at *ca.* 125 kJ mol^{-1} for 10Cu-AE, 20Cu-AE, 25Cu-AE and 30Cu-AE with sufficient Cu^+ sites (denoted as Cu^+-suf); and the higher value at *ca.* 160 kJ mol^{-1} for 25Cu-IM, Cu-SP and 40Cu-AE with sufficient Cu^0 sites (denoted as Cu^0-suf). Interestingly, E_a dropped from 164.5 to 124.5 kJ mol^{-1} when the Cu^0 sites in Cu-SP were oxidized to Cu^+ by N_2O to obtain Cu-SP-N. These results demonstrate the determinant role of the sufficient Cu^+ sites for reaction paths. Herein, 30Cu-AE follows the same reaction path as the other Cu^+-suf catalysts, while its r_{H_2} diverged from that of group I in Fig. 4A, which is probably ascribed to the excessive Cu^0 sites on 30Cu-AE for H_2 desorption. Summarily, we propose that there exist two reaction paths, and which to follow is determined by Cu^+.

Thereafter, we evaluated *in situ* DRIFTS and temperature programmed surface reaction-mass spectroscopy (TPSR-MS) for methanol SR to validate the role of the copper species in the

reaction path. In Fig. 5A, we observe the bands of Cu^+–OCH_3 (methoxy) (1440 cm^{-1}) over Cu^+-suf and Cu^0–OOCH (formate) (1345 cm^{-1}) over Cu^0-suf, respectively, which is also evidenced by the steady-state TPSR-MS (Fig. 5B and C). This suggests that the methoxy and formate groups on their corresponding catalysts are relatively stable, and their dehydrogenation affects the overall reaction rate. Importantly, dioxomethylene (CH_2O_2) is also detected by TPSR-MS in Fig. 5C. Along with the kinetics and E_a discrimination from Fig. 4, these findings demonstrate the different rate-determining steps: methoxy dehydrogenation for Cu^+-suf and formate dehydrogenation for Cu^0-suf.

Then we collected time-resolved *in situ* DRIFTS spectra of 25Cu-AE, Cu-SP and Cu-SP-N (Fig. S15–S17, Table S6†) to draw the hypothetical mechanism. Over Cu^+-suf, we assume that the Cu^0 sites are responsible for transferring atomic H and hydrogen desorption; and the Cu^+ sites contributed to adsorbing oxygen-bonded intermediates.[41] From the *in situ* DRIFTS results in Fig. S15,† the catalytic cycle begins with the dissociative adsorption of methanol (1008 and 1033 cm^{-1}) on the surface. Then, dehydrogenation of the methoxy group (1440 and 1423 cm^{-1}) to formaldehyde occurs as the first barrier. Surface hydroxyls (3737 cm^{-1}) immediately attack the formaldehyde, resulting in the formation of dioxomethylene as a reaction intermediate, whereafter, it dehydrogenates into formate groups (1548 and 1600 cm^{-1}) and proceeds to dehydrogenate eventually to CO_2 (2359 and 2327 cm^{-1}), adsorbing in the form of monodentate carbonate species (1463 cm^{-1}). All H atoms produced by dehydrogenation migrate to the Cu^0 sites through support due to the back spillover, and finally desorb as gaseous H_2. We name it a dual-site reaction path (Fig. 5D). Over Cu^0-suf in Fig. S16,† the adsorption and transition of methanol (1010 and 1030 cm^{-1}), formaldehyde (1736 cm^{-1}), dioxomethylene, formate (1345 and 1577 cm^{-1}) and carbonate (1371 cm^{-1}) occurs on the Cu^0 sites alone (Fig. 5E), consistent with the reported DFT calculations on $Cu(111)$.[42] In this case, H is competitively adsorbed with oxygenated intermediates, thereby readily meeting the second barrier at formate dehydrogenation and inhibiting the overall reaction rate.

Interestingly, in Fig. 5A, monodentate formate (1600 cm^{-1}), considered to be more active in deep dehydrogenation,[43] tends to form on Cu^+-suf, while both monodentate (1577 cm^{-1}) and bidentate (1345 cm^{-1}) species appear on Cu^0-suf. Cu^+ sites may function as the electrophilic sites to readily electrostatically adsorb the negative electron of O–C in formate, thereby forming more active monodentate formate to overcome the formate dehydrogenation barrier. Thus, we intrinsically reveal that the rate-determining step of the dehydrogenation of methoxy or formate relies on the valence state of Cu.

Through the evaluation on a recycle fixed-bed reactor (Fig. S18†), a microkinetic model for methanol SR over 25Cu-AE was established to verify the reliability of our proposed dual-site reaction path (see details in the Experimental section of the ESI†). In this model, the competitive adsorption of oxygenates and dissociative adsorption of hydrogen occur on Cu^+ and Cu^0 sites, respectively. The dehydrogenation of the methoxy group on Cu^+ sites is the rate-determining step, and thus all of the other elemental reactions are in thermodynamic equilibrium.
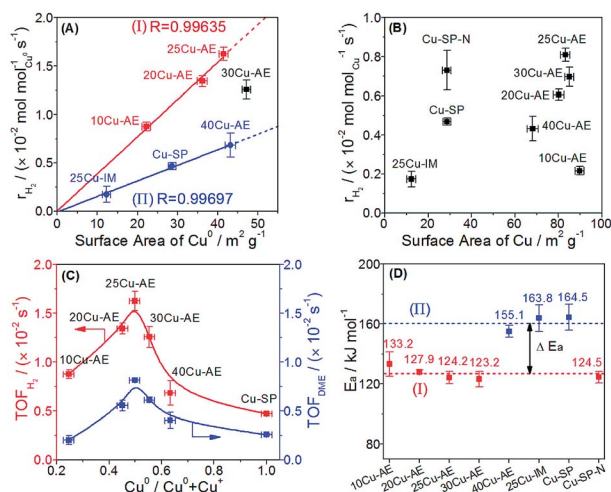

Fig. 4 Correlation of the H_2 production rate based on Cu^0 sites or total Cu sites with (A) the surface area of Cu^0 and (B) total surface area of Cu; (C) correlation of the TOF of H_2 and DME with the $Cu^0/(Cu^0 + Cu^+)$ ratio; (D) apparent activation energies of the catalysts.
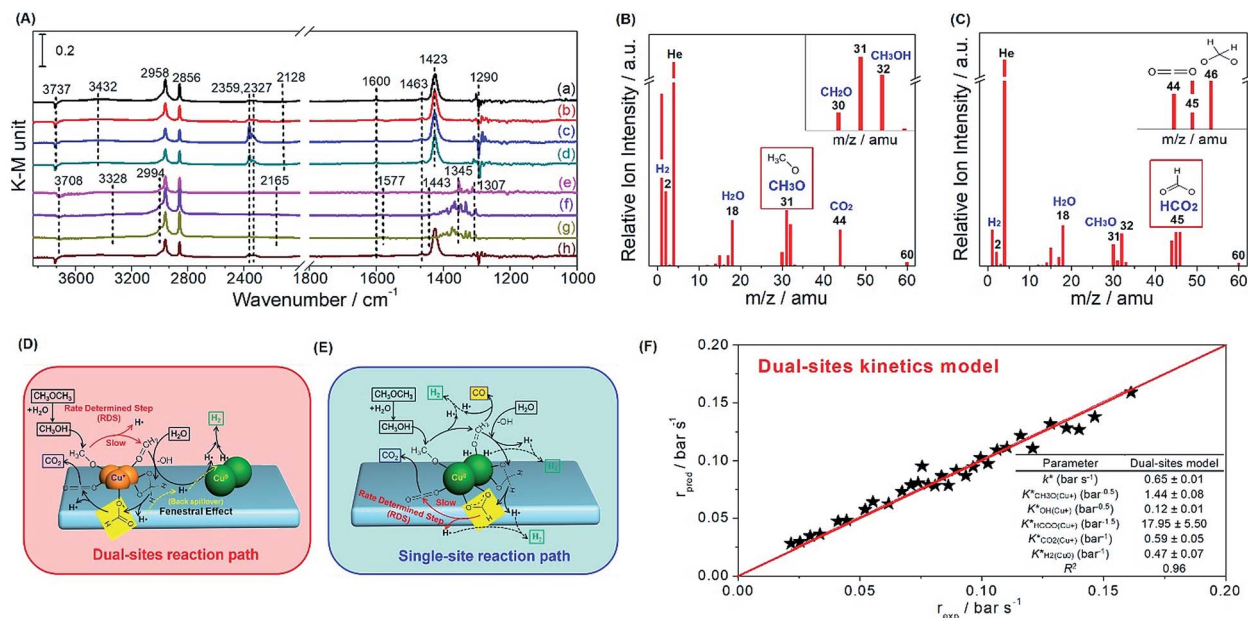
Fig. 5 (A) Steady-state DRIFTS spectra for methanol SR on reduced (a) 10Cu-AE, (b) 20Cu-AE, (c) 25Cu-AE, (d) 30Cu-AE, (e) 40Cu-AE, (f) 25Cu-IM, and (g) Cu-SP, and (h) Cu-SP-N; TPSR-MS spectra for methanol SR over the (B) reduced 25Cu-AE (Cu^+-suf) and (C) Cu-SP (Cu^0-suf) at 230 °C under steady-state conditions; the hypothetical reaction paths on the (D) dual-sites of copper species; and (E) single Cu^0 site; (F) parity plots of microkinetic modeling for methanol SR over 25Cu-AE, and the inset shows the fitting parameters given with the confidence interval (±5%) and stability index R^2.

As expected, the experimental data and the dual-site microkinetic prediction are in good agreement (Fig. 5F).

Conclusions

In summary, we have successfully designed a dual Cu reforming system with a record-high and robust H_2 production rate of 1145 mol kg_{cat}^{-1} h^{-1}, and provided new insights into the fundamental understanding of Cu-catalyzed SR. In fact, there exist two kinds of distinct rate-determining steps: methoxy dehydrogenation for Cu^+-suf and formate dehydrogenation for Cu^0-suf. Cu^+ may function as the electrophilic site to adsorb the negative electron of O–C in formate, thereby more readily forming active monodentate formate. This can intrinsically accelerate the overall reaction rates. Moreover, the surrounding Cu_2O and nano-channels of SBA-15 can inhibit the aggregation of metallic Cu species during SR. Our design provides a commercially achievable reforming system for fuel cells and paves a new way to related reaction mechanism investigations.

Conflicts of interest

The authors declare no conflict of interest.

Author contributions

X. G. L., J. L. G. and K. M. conceived the idea; K. M., J. L. G., Y. T., Z. J. Z., Q. P. C. and T. D. carried out the experiments; N. T. and T. A. prepared the sputtered catalysts; J. Z., L. R. Z. and Z. J. helped collect XAFS data; X. G. L., J. L. G. and K. M. analyzed the experimental data and wrote the manuscript. X. G. L. and J. L. G. supervised the whole project. All authors participated in discussions of the research.

Acknowledgements

Notes and references

1 M. Dresselhaus and I. Thomas, *Nature*, 2001, **414**, 332–337.
2 U. Eberle, B. Muller and R. von Helmolt, *Energy Environ. Sci.*, 2012, **5**, 8780–8798.
3 S. Krishnan and F. A. Armstrong, *Chem. Sci.*, 2012, **3**, 1015–1023.
4 R. D. Cortright, R. Davda and J. A. Dumesic, *Nature*, 2002, **418**, 964–967.
5 L. Schlapbach and A. Züttel, *Nature*, 2001, **414**, 353–358.
6 P. Leung, A. Tsolakis, J. Rodriguez-Fernandez and S. Golunski, *Energy Environ. Sci.*, 2010, **3**, 780–788.
7 C. Dang, Y. Li, S. M. Yusuf, Y. Cao, H. Wang, H. Yu, F. Peng and F. Li, *Energy Environ. Sci.*, 2018, **11**, 660–668.

8 X. Zhao, H. Zhou, V. S. Sikarwar, M. Zhao, A.-H. A. Park, P. S. Fennell, L. Shen and L.-S. Fan, *Energy Environ. Sci.*, 2017, **10**, 1885–1910.

9 T. A. Semelsberger, R. L. Borup and H. L. Greene, *J. Power Sources*, 2006, **156**, 497–511.

10 J. Sun, G. Yang, Y. Yoneyama and N. Tsubaki, *ACS Catal.*, 2014, **4**, 3346–3356.

11 R. Luque, L. Herrero-Davila, J. M. Campelo, J. H. Clark, J. M. Hidalgo, D. Luna, J. M. Marinas and A. A. Romero, *Energy Environ. Sci.*, 2008, **1**, 542–564.

12 K. Faungnawakij, R. Kikuchi, N. Shimoda, T. Fukunaga and K. Eguchi, *Angew. Chem., Int. Ed.*, 2008, **47**, 9314–9317.

13 D. Li, X. Li and J. Gong, *Chem. Rev.*, 2016, **116**, 11529–11653.

14 D. R. Palo, R. A. Dagle and J. D. Holladay, *Chem. Rev.*, 2007, **107**, 3992–4021.

15 H. Oguchi, T. Nishiguchi, T. Matsumoto, H. Kanai, K. Utani, Y. Matsumura and S. Imamura, *Appl. Catal., A*, 2005, **281**, 69–73.

16 Y. Matsumura and H. Ishibe, *J. Catal.*, 2009, **268**, 282–289.

17 Y. Matsumura and H. Ishibe, *Appl. Catal., B*, 2009, **86**, 114–120.

18 I. Ritzkopf, S. Vukojević, C. Weidenthaler, J.-D. Grunwaldt and F. Schüth, *Appl. Catal., A*, 2006, **302**, 215–223.

19 Y. Liu, T. Hayakawa, K. Suzuki, S. Hamakawa, T. Tsunoda, T. Ishii and M. Kumagai, *Appl. Catal., A*, 2002, **223**, 137–145.

20 X. Wang, K. Ma, L. Guo, Y. Tian, Q. Cheng, X. Bai, J. Huang, T. Ding and X. Li, *Appl. Catal., A*, 2017, **540**, 37–46.

21 C. Rameshan, W. Stadlmayr, S. Penner, H. Lorenz, N. Memmel, M. Hävecker, R. Blume, D. Teschner, T. Rocha, D. Zemlyanov, A. Knop-Gericke, R. Schlögl and B. Klötzer, *Angew. Chem., Int. Ed.*, 2012, **51**, 3002–3006.

22 K. M. K. Yu, W. Tong, A. West, K. Cheung, T. Li, G. Smith, Y. Guo and S. C. E. Tsang, *Nat. Commun.*, 2012, **3**, 1230.

23 J. Huang, T. Ding, K. Ma, J. Cai, Z. Sun, Y. Tian, Z. Jiang, J. Zhang, L. Zheng and X. Li, *ChemCatChem*, 2018, **10**, 3862–3871.

24 H. Xi, X. Hou, Y. Liu, S. Qing and Z. Gao, *Angew. Chem., Int. Ed.*, 2014, **53**, 11886–11889.

25 K. Ma, Z. Cui, Z. Zhang, J. Huang, Z. Sun, Y. Tian, T. Ding and X. Li, *ChemCatChem*, 2018, **10**, 4010–4017.

26 L. F. Chen, P. J. Guo, M. H. Qiao, S. R. Yan, H. X. Li, W. Shen, H. L. Xu and K. N. Fan, *J. Catal.*, 2008, **257**, 172–180.

27 J. Gong, H. Yue, Y. Zhao, S. Zhao, L. Zhao, J. Lv, S. Wang and X. Ma, *J. Am. Chem. Soc.*, 2012, **134**, 13922–13925.

28 H. Yue, Y. Zhao, S. Zhao, B. Wang, X. Ma and J. Gong, *Nat. Commun.*, 2013, **4**, 2339.

29 R. Van den Berg, T. E. Parmentier, C. F. Elkjær, C. J. Gommes, J. Sehested, S. Helveg, P. E. de Jongh and K. P. de Jong, *ACS Catal.*, 2015, **5**, 4439–4448.

30 J. Fan, X. Jiang, H. Min, D. Li, X. Ran, L. Zou, Y. Sun, W. Li, J. Yang, W. Teng, G. Li and D. Zhao, *J. Mater. Chem. A*, 2014, **2**, 10654–10661.

31 T. Tsoncheva, V. Dal Santo, A. Gallo, N. Scotti, M. Dimitrov and D. Kovacheva, *Appl. Catal., A*, 2011, **406**, 13–21.

32 X. Wang, J. Zhuang, J. Chen, K. Zhou and Y. Li, *Angew. Chem., Int. Ed.*, 2004, **116**, 2051–2054.

33 A. Ungureanu, B. Dragoi, A. Chirieac, C. Ciotonea, S. Royer, D. Duprez, A. S. Mamede and E. Dumitriu, *ACS Appl. Mater. Interfaces*, 2013, **5**, 3010–3025.

34 L. F. Chen, P. J. Guo, L. J. Zhu, M. H. Qiao, W. Shen, H. L. Xu and K. N. Fan, *Appl. Catal., A*, 2009, **356**, 129–136.

35 A. Marchi, J. Fierro, J. Santamaria and A. Monzon, *Appl. Catal., A*, 1996, **142**, 375–386.

36 A. Yin, X. Guo, W. L. Dai and K. Fan, *J. Phys. Chem. C*, 2009, **113**, 11003–11013.

37 X. Zheng, H. Lin, J. Zheng, X. Duan and Y. Yuan, *ACS Catal.*, 2013, **3**, 2738–2749.

38 L. S. Kau, D. J. Spira-Solomon, J. E. Penner-Hahn, K. O. Hodgson and E. I. Solomon, *J. Am. Chem. Soc.*, 1987, **109**, 6433–6442.

39 Y. Tanaka, R. Kikuchi, T. Takeguchi and K. Eguchi, *Appl. Catal., B*, 2005, **57**, 211–222.

40 X. G. Li, C. Liu, J. Sun, H. Xian, Y. S. Tan, Z. Jiang, A. Taguchi, M. Inoue, Y. Yoneyama, T. Abe and N. Tsubaki, *Sci. Rep.*, 2013, **3**, 2813.

41 S. Lin, D. Xie and H. Guo, *J. Phys. Chem. C*, 2011, **115**, 20583–20589.

42 S. Lin, R. S. Johnson, G. K. Smith, D. Xie and H. Guo, *Phys. Chem. Chem. Phys.*, 2011, **13**, 9622–9631.

43 A. Haghofer, D. Ferri, K. Föttinger and G. n. Rupprechter, *ACS Catal.*, 2012, **2**, 2305–2315.